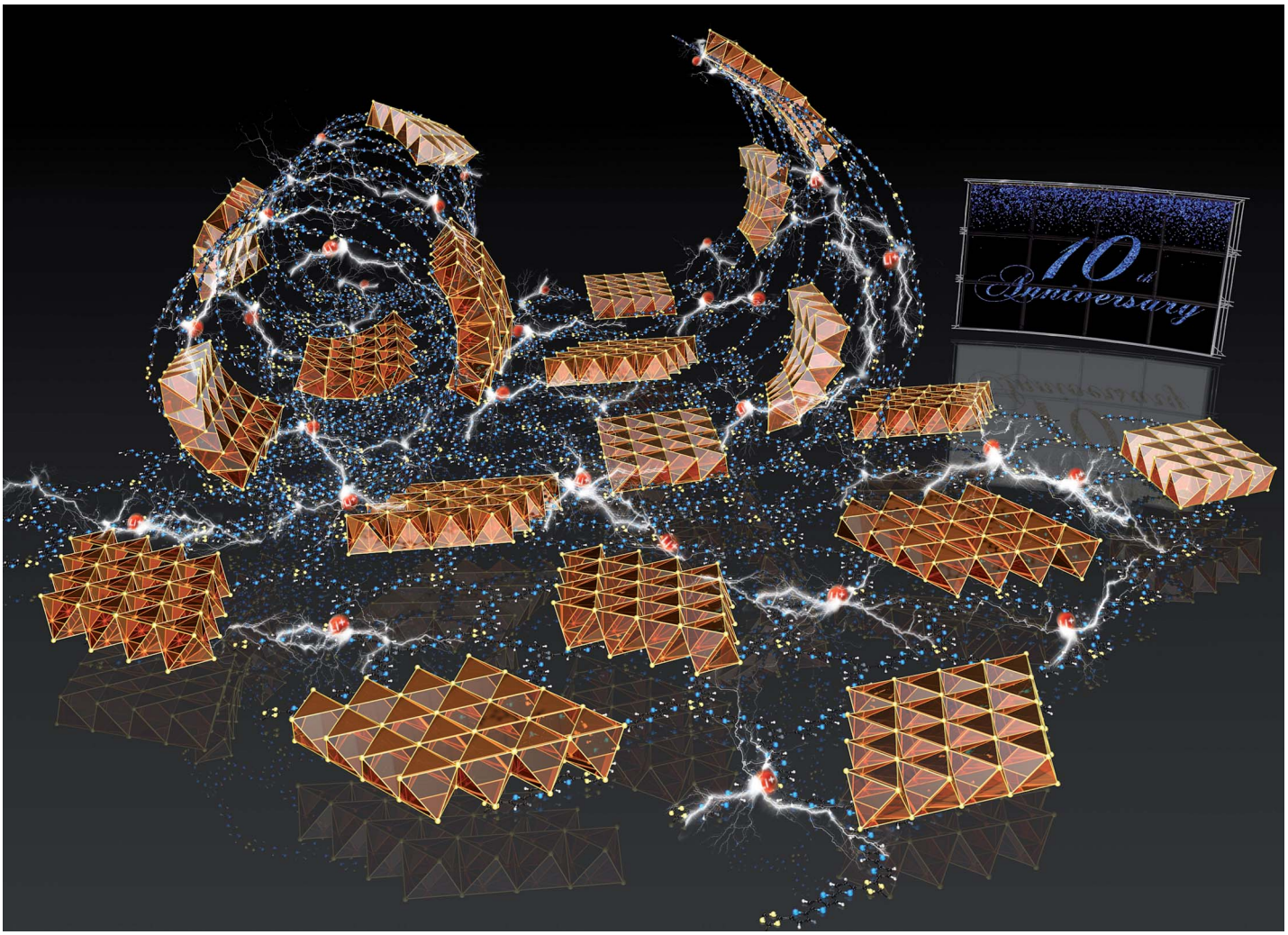

Showcasing research on SnS_2-based covalent organic nanosheet by a group of researchers led by Dr. Jung-Hun Jang, Mr. Minseop Lee, and Prof. Seung-Min Paek (from Kyungpook National University), and Mr. Soohyeon Park and Prof. Jin Kuen Park (from Hankuk University of Foreign Studies), and Prof. Jae-Min Oh (from Dongguk University).

Long-term cycling stability of a SnS_2-based covalent organic nanosheet anode for lithium-ion batteries

The hybrid electrode improves performances of lithium ion batteries for long charge/discharge cycles.

As featured in:

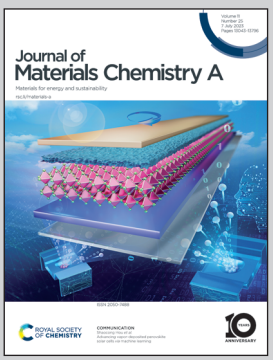

See Jae-Min Oh, Jin Kuen Park, Seung-Min Paek *et al.*, *J. Mater. Chem. A,* 2023, **11**, 13320.

ROYAL SOCIETY OF CHEMISTRY

rsc.li/materials-a

Registered charity number: 207890

Journal of Materials Chemistry A

ROYAL SOCIETY OF CHEMISTRY

PAPER

View Article Online
View Journal | View Issue

Cite this: J. Mater. Chem. A, 2023, 11, 13320

Long-term cycling stability of a SnS_2-based covalent organic nanosheet anode for lithium-ion batteries†

Jeong-Hun Jang,[a] Minseop Lee,[a] Soohyeon Park,[b] Jae-Min Oh, *[c] Jin Kuen Park *[b] and Seung-Min Paek *[a]

Received 14th March 2023
Accepted 24th May 2023

DOI: 10.1039/d3ta01537h

rsc.li/materials-a

Various SnS_2-based carbonaceous anodes for lithium ion battery (LIB) systems have been developed to enhance the electrochemical performance of SnS_2 materials and to overcome the disadvantages of transition metal sulfides with less interfacial surface sites and low electrochemical conductivity. In this study, we introduced a new strategy of hybridization of SnS_2 and covalent organic nanosheets (CONs) that have high flexibility, high stability in organic electrolytes, and many interfacial surface sites. The CON provided reaction sites for the growth of SnS_2 nanoparticles due to the strong electrostatic interaction between the sulfur heteroatoms of CONs and Sn^{4+}, resulting in the formation of ultrathin SnS_2 nanoplates on the CON nanosheets. The resulting SnS_2-based CON showed outstanding cyclic stability over 5600 charge/discharge cycles at a current density of 1.0 A g^{-1} in the LIB system. In particular, the prominent interfacial surface sites of CONs provided large accessible areas for lithium ions, showing stable successive cycling performances with improved electrical and ionic conductivities.

Introduction

The growing demand for energy storage devices ranging from portable smart devices to various electric vehicles has led to extensive worldwide research on the development of advanced secondary batteries.[1] For this purpose, SnS_2 has been widely concerned as one of the promising anode materials for lithium-ion battery (LIB) systems since SnS_2 has various desirable properties for energy storage systems, such as non-toxicity, high lithium storage capacity, and low cost.[2] Nevertheless, its large volume change in its bulk solid state during discharge/charge cycling has resulted in cracks and pulverization on its surface, which has limited the broad application of SnS_2 as the anode material.[3] To overcome such drawbacks of SnS_2 as the anode material, one of the widely accepted strategies is the employment of carbonaceous materials on SnS_2-based systems, which can alleviate the undesirable volume change of SnS_2 and show high electrochemical performances. Furthermore, since the carbonaceous materials with high electrical and ionic conductivities can be easily and cost-effectively prepared, they have attained great attention as promising adjuvant materials to improve the electrochemical energy storage properties of SnS_2.[4–8]

Several successful attempts have been made *via* coating SnS_2 particles with a wide variety of carbonaceous materials[9,10] such as highly conductive carbon,[11] carbon nanotubes,[12] and carbon nanoboxes.[13] However, their rigid structures and weak interactions of SnS_2 particles with carbonaceous materials resulted in a gradual decrease in Li-storage capacity during discharge/charge cycling. Therefore, such SnS_2-based carbonaceous systems have been further modified for achieving stable energy storage performances. In this regard, several systems as anodes in LIBs have been suggested. For example, a nanocomposite between SnS_2 and multiwalled carbon nanotubes exhibited a Li-storage capacity of 518 mA h g^{-1} at a current density of 0.1 A g^{-1}.[14] Furthermore, polypyrrole-encapsulated SnS_2 nanosheets stabilized with defected TiO_2 showed a Li-storage capacity of 508.7 mA h g^{-1} up to 2000 cycles at a current density of 2.0 A g^{-1}.[15] However, the fabrication of such nanocomposites required an elaborate and time-consuming synthesis process. Besides, their low electrical conductivities and ionic conductivities still demand new types of alternative carbonaceous materials for the inorganic components in functioning LIB systems.

In this regard, covalent organic nanosheets (CONs) as a 2-dimensional analogue of covalent organic frameworks (COFs) are considered to be excellent candidates for anode materials in LIBs owing to their high flexibility, facile designability, superior energy density, and high electrical conductivity.[16–19] For example, CONs with variable porosity and tuneable network connectivity can be utilized as electrode materials for secondary

[a]Department of Chemistry, Kyungpook National University, Daegu 41566, Republic of Korea. E-mail: smpaek@knu.ac.kr

[b]Department of Chemistry, Hankuk University of Foreign Studies, Yongin, 17035, Gyeonggi-do, Republic of Korea. E-mail: jinkpark@hufs.ac.kr

[c]Department of Energy and Materials Engineering, Dongguk University-Seoul, Seoul 04620, Republic of Korea. E-mail: jaemin.oh@dongguk.edu

† Electronic supplementary information (ESI) available: Additional instrumental and theoretical characterizations of CONs. See DOI: https://doi.org/10.1039/d3ta01537h

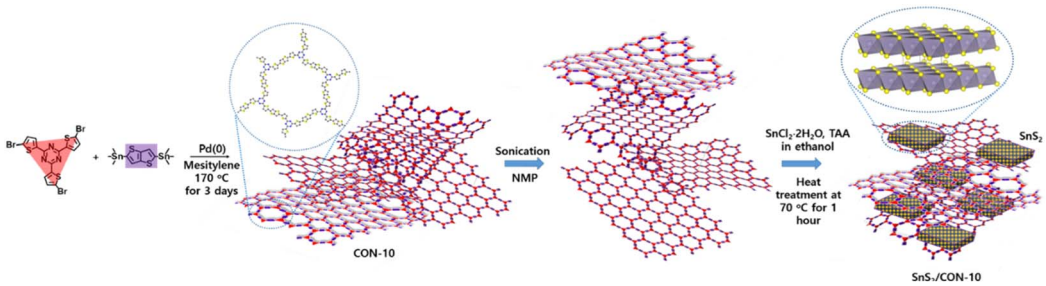

Scheme 1 The schematic illustration of the procedure to synthesize SnS_2/CON-10.

batteries.[17–19] Generally, the high solubility of organic anode materials in electrolytes has been concerned as a disadvantage, which results in poor cycling performance of electrodes. On the other hand, CONs showed excellent cyclability upon successive charge/discharge reactions due to their high stability in electrolytes.[18,19] 3-Dimensional (3D) COFs also have abundant interfacial surface sites, but it is hard to obtain exfoliated nanosheets from 3D-COFs because most of the conventional 3D-COFs have organic linkers that form covalent bonds between building units. These drawbacks of 3D-COFs could restrict their application in LIBs as carbonaceous additives for inorganic components such as SnS_2, whereas CONs have minimized intermolecular interactions between them so that they could form a stable colloidal suspension. In previous research, we characterized the exfoliated structures of CONs in a suitable solvent and established a proper synthetic method to obtain exfoliated CONs consisting of thin layers.[20,21] Furthermore, the electrical and ionic conductivities of CONs as anodes in LIBs can be finely controlled by choosing various aromatic derivatives such as triazine, thiophenes and benzenes.[18] Also, CONs could be facile building blocks to fabricate nanocomposites between organic and inorganic components.[22] Meanwhile, a simple one pot strategy was suggested to synthesize a SnS_2-based graphene nanocomposite.[23] The resulting anode material showed high lithium storage capacity because of the well-dispersed SnS_2 nanoparticles within graphene matrices. Inspired by this method in the previous literature, we propose that SnS_2 nanoparticles could be homogeneously formed in between the matrices of CONs by using the intermolecular van der Waals forces between SnS_2 and CONs. Moreover, highly conjugated and delocalized backbones in CONs would contribute to improve the electrical and ionic conductivity. From these reasons, SnS_2-based CONs could be a new strategy to enhance the electrochemical properties of CONs with high lithium storage capacity and cycling stability by the synergic roles of CONs and SnS_2 nanoparticles.

In this study, as a representative CON framework, CON-10 was used, which can be prepared *via* a Stille cross-coupling polymerization between 2,5-bis(trimethyl-stannyl)thieno-(3,2-*b*)thiophene and 2,4,6-tris(5-bromo-thiophenyl-2-yl)-1,3,5-triazine.[17–21] Subsequently, to induce the intra-growth of SnS_2 nanoparticles within the matrices of CON-10, all precursors and reagents for synthesizing SnS_2 were added in the *N*-methyl-2-pyrrolidone (NMP) suspension of the as-prepared CON-10, as shown in Scheme 1. Then, the reaction system was in progress for 1 hour under the right conditions for the synthesis of SnS_2. Then, the obtained materials after purification were investigated to define the structures of SnS_2-based CON-10 (SnS_2/CON-10) and electrochemical performances with the goal of establishing the relationship between their chemical structures and observed energy storage properties.

Results and discussion

To investigate structural integrity, we observed the powder X-ray diffraction (XRD) patterns of samples, as shown in Fig. 1. The XRD patterns of SnS_2/CON-10 (Fig. 1) and bare SnS_2 (Fig. 1c) revealed broad peaks at 2θ degree of around 30 and 50. These two broad peaks of SnS_2/CON-10 and bare SnS_2 would correspond to the sum of (100) and (002) peaks at 2θ degree of around 30 and another sum of (110) and (113) peaks at 2θ degree of around 50, respectively, implying a hexagonal SnS_2 structure.[7,9,23] Therefore, the broad XRD features of SnS_2/CON-10 and bare SnS_2 would originate from the weak crystallinity rather than amorphous features, which would be derived from small particle size and stacking faults of crystals.[24] On the other hand, the weak and broad feature in the XRD pattern of pristine CON-10 in the 2θ degree range from 20 to 25 could be indexed to the representative pattern of disordered π–π stacking of two dimensional (2D) organic materials along the crystallographic *c*-axis (Fig. 1a). In this regard, we supposed that the synthesized SnS_2/CON-10 showed structural characteristics of both bare SnS_2 and pristine CON-10, showing that SnS_2/CON-10 was successfully synthesized as shown in Scheme 1.

Solid-state UV-vis spectra were examined to clarify the electronic features of samples (Fig. 1d). The semiconducting properties of SnS_2/CON-10 showed significant differences from those of bare SnS_2. Differences in the optical bandgaps of SnS_2/CON-10 and bare SnS_2 were analyzed by converting UV-Vis absorption spectra to the Tauc plot based upon $(ahv)^2$ and photon energy (hv) relationship (Fig. 1e and f). First of all, it was confirmed that the broad absorption edge of SnS_2/CON-10 in UV-Vis spectra was significantly red-shifted with respect to that of SnS_2, indicating that the optical bandgap of SnS_2/CON-10 was narrower than that of bare SnS_2 (Fig. 1f). The calculated bandgaps of bare SnS_2 and SnS_2/CON-10 were found to be 1.93 and 1.70 eV, respectively (Fig. 1e and f). In addition, SnS_2/CON-10 not only showed a significantly reduced bandgap compared

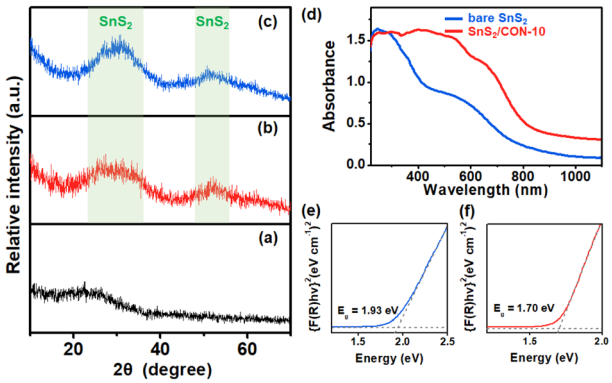

Fig. 1 XRD patterns of (a) CON-10, (b) SnS_2/CON-10, and (c) bare SnS_2; (d) solid-state UV-vis absorption spectra of bare SnS_2 (blue), and SnS_2/CON-10 (red); the bandgap energy (E_g) of (e) bare SnS_2, and (f) SnS_2/CON-10 estimated from the Tauc plot.

to bare SnS_2 but also showed much higher light absorption in the visible light region, highlighting the presence of CON-10 in the matrices of SnS_2.[17,19] These results would imply a new heterostructured nanocomposite consisting of 2D inorganic (SnS_2) and organic materials (CON-10).

Fig. 2 compares the Raman spectra of samples in the range from 100 to 2000 cm^{-1}. The Raman spectrum (Fig. 2a, black line) of bare SnS_2 displayed a distinct peak at 315 cm^{-1}, which corresponds to the A_{1g} mode of SnS_2,[25] whereas the specific A_{1g} mode was hardly discernible in both those of SnS_2/CON-10 (Fig. 2a, red line) and of CON-10 (Fig. 2a, blue line). The intensity of A_{1g} mode is known to be sensitive to the layer thickness of SnS_2.[26] Therefore, such negligible A_{1g} mode in the Raman spectrum of SnS_2/CON-10 could imply that very thinner and smaller size SnS_2 particles were formed in the matrices of the CON layers than in bare SnS_2. Therefore, it could be worth noting that the internal structure of the hybrid would be postulated as described in Scheme 1. In addition, we also investigated FT-IR spectra to reveal the structural characteristics of SnS_2 in SnS_2/CON-10 (Fig. 2b). Both of bare SnS_2 and SnS_2/CON-10 spectra developed a broad peak at *ca.* 550 cm^{-1} corresponding to the Sn–S vibrational mode in SnS_2. Meanwhile, other vibrational modes in the SnS_2/CON-10 spectrum were derived from CON-10, which is in good agreement with the reported results in the previous literature (Fig. 2b, blue profile).[17,20]

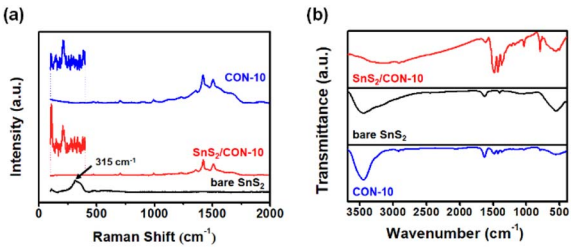

Fig. 2 (a) Raman spectra of bare SnS_2 (black), SnS_2/CON-10 (red), and CON-10 (blue); (b) Fourier transform-infrared (FTIR) spectra of CON-10 (blue), bare SnS_2 (black) and SnS_2/CON-10 (red).

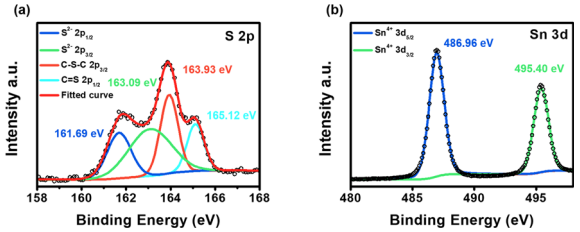

Fig. 3 High-resolution XPS spectra of SnS_2/CON-10 for (a) S 2p and (b) Sn 3d.

The formation of SnS_2 species within CON-10 matrices was also probed using XPS spectra (Fig. 3). The high-resolution S 2p spectrum was deconvoluted to four peaks, in which each peak was assigned to be 161.69, 163.09, 163.94, and 165.12 eV, as illustrated in Fig. 3a. The binding energies of 161.69 and 163.09 eV could correspond to electrons in the S $2p_{1/2}$ and S $2p_{3/2}$ orbitals of S_2^-, respectively, which originate from SnS_2 phases.[27,28] The binding energies of 163.93 and 165.12 eV can be assigned to electrons in S $2p_{3/2}$ of C–S–C bonds and S $2p_{1/2}$ of C=S bonds, respectively, which originate from CON-10 phases, as confirmed in Fig. S1.† Meanwhile, the high-resolution Sn 3d spectrum showed two distinct peaks at binding energies of 486.96 and 495.40 eV corresponding to Sn $3d_{5/2}$ and Sn $3d_{3/2}$ of Sn^{4+}, respectively, which are also from SnS_2 phases.[27,28] In addition, X-ray absorption spectroscopy (XAS) data for SnS_2/CON-10 was virtually identical to that of bare SnS_2 (Fig. S2†). Such XPS and XAS spectra clearly described that SnS_2 was successfully formed in SnS_2/CON-10.

The images from scanning electron microscopy (SEM) could show the direct morphological evolution of each phase in SnS_2/CON-10, as shown in Fig. 4. The SEM images of bare SnS_2 (Fig. 4a and b) exhibited aggregated globular particles. On the other hand, the SEM images of CON-10 and SnS_2/CON-10

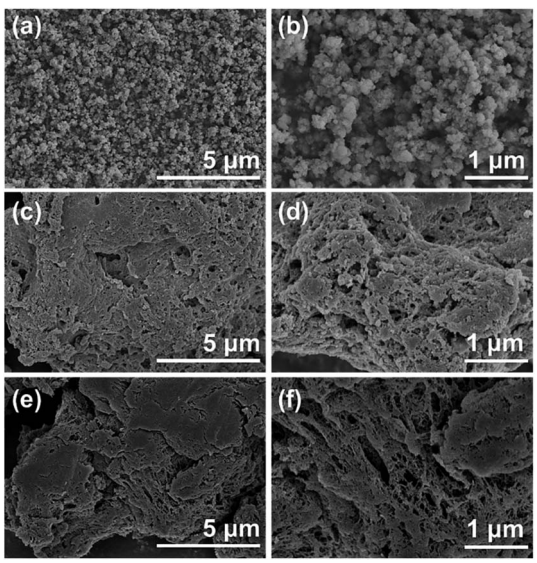

Fig. 4 SEM images of (a, b) bare SnS_2, (c, d) SnS_2/CON-10, and (e, f) CON-10.

showed randomly stacked plate-like morphologies (Fig. 4 from c to f). However, the tiny globular particles were not observed in the image of SnS_2/CON-10, implying that the SnS_2 particles were formed on the nanoscale within CON-10 frameworks (Fig. 4c and d). From the thermogravimetric analysis (TGA) as shown in Fig. S3,† we calculated the content of SnS_2 within SnS_2/CON-10.[23] The weight loss from 200 to 800 °C in Fig. S3† was mainly derived from carbon combustion and the formation of SnO_2. The weight percent of SnS_2 in SnS_2/CON-10 was calculated to be 72.05%. In spite of such a considerable amount of SnS_2 in SnS_2/CON-10, the morphology of SnS_2/CON-10 which was similar to that of pristine CON-10 rationally implied that nanosized SnS_2 particles were well-dispersed in between flexible CON-10 frameworks.

Transmission electron microscope (TEM) analysis was performed to elucidate the local structural features such as lattice fringes in SnS_2/CON-10 (Fig. 5). As shown in Fig. 5a, it was found that tiny SnS_2 particles in dark domains were distributed through the CON-10 sheets because the magnified dark domains showed clear lattice fringes (Fig. 5b). Then, the sizes of SnS_2 particles were measured in several nanometers from the magnified the TEM image, as suggested by the XRD and Raman results. The lattice fringes with a spacing of 0.32 nm in the high-magnification TEM image (indicated by green rectangles of 5 and 6 in Fig. 5b) correspond to (100) planes of SnS_2. Besides, in Fig. 5b, the interlayer spacing of CON-10 (indicated by yellow-coloured rectangles of 1–4) was calculated to be around 0.38–0.53 nm, which was larger than that of SnS_2 for the (100) plane; especially, the quite variable *d*-spacing of CON-10 could imply the flexibility of CONs. Furthermore, the EDS-mapping images (Fig. 5c–g) of SnS_2/CON-10 revealed that the Sn element was well distributed in the CON-10 framework represented with C and S elements; especially, upon merging C and Sn element maps (Fig. 5g), the domains where Sn element was intensely detected were well matched to bright regions from the high-angle annular dark field scanning transmission electron microscope (HAADF-STEM) image, as shown in Fig. 5c. The bright spots in the HAADF-STEM image were also well matched to the dark spots in the TEM images. Furthermore, as shown in Fig. S4,† the surface area of SnS_2/CON-10 was 72 $m^2\ g^{-1}$, while that of CON-10 is 202 $m^2\ g^{-1}$,[18] indicating that SnS_2 nanoparticles filled the pores developed by secondary particles of CON-10. Therefore, we confirmed that SnS_2 nanoparticles were successfully formed within the matrices of CON-10 frameworks. Furthermore, it could be rationally suggested that the SnS_2 phases would be well formed in between the CON-10 sheets, as illustrated in Scheme 1. However, a specific order was not found in the arrangement of SnS_2 particles and some possible chemical bonds were not found between SnS_2 particles and CONs, as shown in the XPS analysis above. Nonetheless, the segregated phases of SnS_2 were not detected either. Therefore, it could be speculated that the driving forces to hybridize SnS_2 particles on the surface of CONs would be ascribed to van der Waals interaction, which is well known as a non-directional force. The ultrafine SnS_2 nanoparticles could desirably improve electrochemical energy storage properties with providing large accessible surface areas, shortening diffusion pathways for Li^+ ions and alleviating the pulverization of materials from the anode during the discharge/charge process.[29–31]

The lithiation/delithiation behaviors of SnS_2/CON-10 and bare SnS_2 electrodes were investigated with cyclic voltammetry (CV) analysis at a scan rate of 0.1 mV s^{-1} for 15 cycles. In the

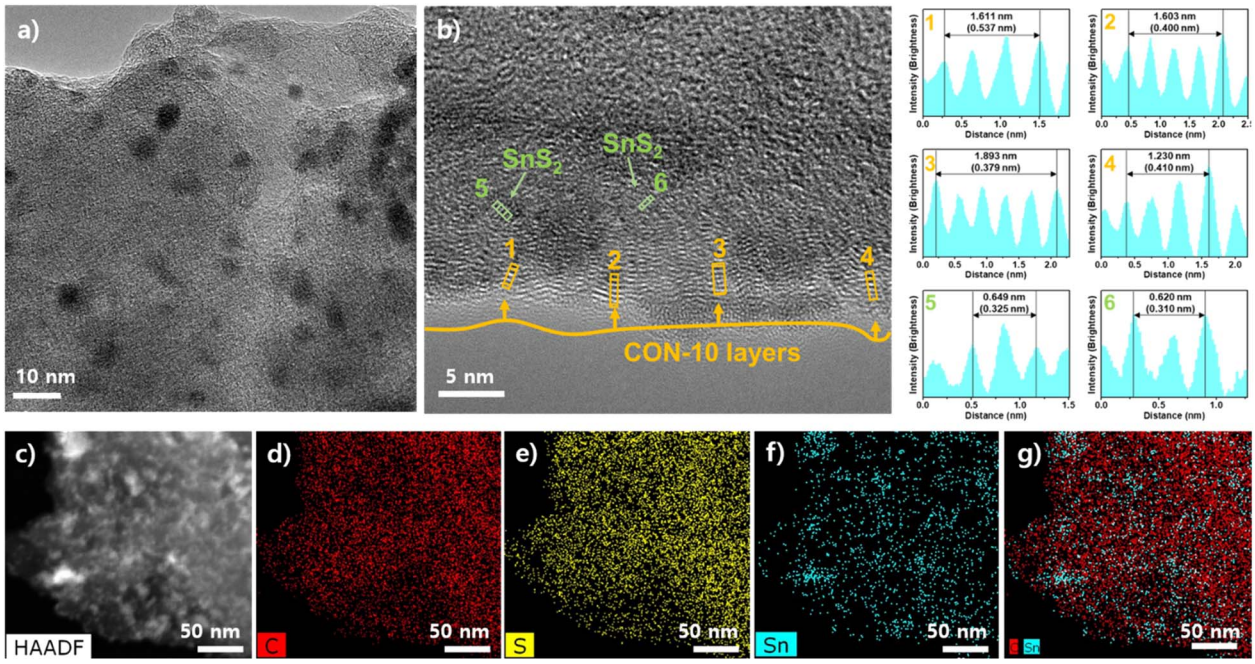

Fig. 5 TEM images of SnS_2/CON-10 at (a) low and (b) high magnification together with brightness profiles from the rectangle areas of (b); (c) HAADF-STEM image for EDS elemental maps of SnS_2/CON-10 (d–g).

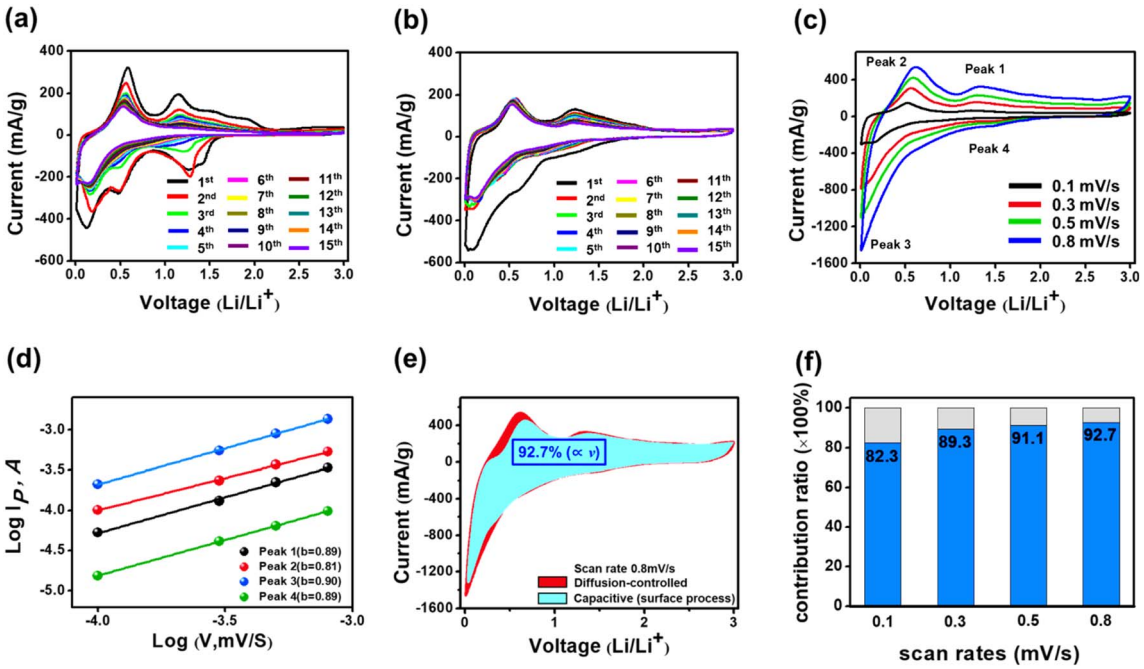

Fig. 6 CV profiles of (a) bare SnS_2 and (b) SnS_2/CON-10 electrodes at a scan rate of 0.1 mV s^{-1}; CV curves at various scan rates from 0.1 to 0.8 mV s^{-1} for the (c) SnS_2/CON-10 electrode; Cottrell plots of (d) the SnS_2/CON-10 electrode; separation of the pseudocapacitive and diffusion-controlled charge-storage process of (e) the SnS_2/CON-10 electrode at 0.8 mV s^{-1}; (f) pseudocapacitive contributions of (e) the SnS_2/CON-10 electrode.

case of the SnS_2/CON-10 electrode (Fig. 6b) at the first scan, the cathodic peaks at 1.28 V were attributed to the decomposition of SnS_2, the formation of Li_2S and solid electrolyte interface (SEI).[32] A broad cathodic peak at 0.6 V was attributed to the formation of Li_xSn alloy. Furthermore, there were two broad anodic peaks at 0.56 V and 1.23 V, which correspond to dealloying reaction and delithiation process, respectively. Overall, the CV curves (Fig. 6b) of SnS_2/CON-10 are analogous with those of bare SnS_2 (Fig. 6a), indicating that the discharge/charge process in the SnS_2/CON-10 electrode predominantly occurred on SnS_2 nanoparticles. At the second scan, the current of the SnS_2/CON-10 electrode was slightly decreased upon the formation of SEI. However, the 5th CV cycle of SnS_2/CON-10 almost identically overlapped with subsequent cycles without further decrease, while none of bare SnS_2 overlapped and exhibited a gradual decrease in current. Thus, this feature clearly highlighted that the SnS_2/CON-10 electrode showed an almost reversible discharge/charge process after the 4th cycle but bare SnS_2 did not reach the reversible stage. Therefore, CV profiles revealed that CON-10 could effectively prevent the large volume changes of SnS_2 nanoparticles during discharge/charge cycles, which is necessarily required for the stable cycling performance of the anode.

The SnS_2/CON-10 electrode that reached the reversible stage after 15 consecutive scans in CV profiles at the sweep rate of 0.1 mV s^{-1} (Fig. 6b) was used for further additional CV measurements at various scan rates from 0.1 to 0.8 mV s^{-1} (Fig. 6c) to clearly analyse the reaction kinetics related to Li-ion storage in this system. As the scan rate increases, the cathodic and anodic peaks gradually broaden because the electrochemical polarization increases (Fig. 6c). The Li-ion storage dynamics were investigated through a relationship between current and scan rate, as shown in eqn (1), with the data empirically obtained from CV measurements.

$$\log i = b \log v + \log a \quad (1)$$

This power-law relationship has two variables of a and b, where the b-value determines the type of charge storage behavior in the delithiation/lithiation process. A b-value close to 1.0 indicates a capacitive process at the electrode surface. In contrast, a b-value close to 0.5 means that the electrochemical energy storage reaction is governed by a diffusion-controlled faradaic process. The b-values (Fig. 6d) were found to be 0.89 (for peak 1), 0.81 (for peak 2), 0.90 (for peak 3) and 0.89 (for peak 4), respectively, indicating that Li-ion storage was mainly determined by the surface storage process.[33,34] In general, the b values of conventional electrodes in LIBs are close to 0.5. However, the hybrid material used in this study showed much higher b values than the conventional anodes, implying the considerably higher contribution of the pseudocapacitive process.[35–37] Although it was still hard to speculate why b values were close to 1 in this specific case, it could be suggested from the CV analysis as displayed in Fig. 6 that Li^+ ions were weakly bound on the polarized surfaces of the hybrid without forming any strong covalent bonds. Furthermore, since the cathodic and anodic currents in all the CV profiles (Fig. 6) were substantially proportional to the square root values of the applied scan rates, the major charge storage mechanism of the hybrid material

used in this study could also be subject to the mass-transfer process.

Then, to quantify and compare the relative contributions of the two kinetic processes in more detail, we distinguished the capacitive process (k_1v) and the diffusion-controlled process ($k_2v^{1/2}$) according to the method previously reported by Dunn *et al.* (eqn (2) and (3)).

$$i(V) = k_1v + k_2v^{1/2} \quad (2)$$

$$i(V)/v^{1/2} = k_2v^{1/2} + k_2 \quad (3)$$

In general, k_1v is classified as the surface-controlled process, such as a pseudocapacitive or non-faradaic capacitive behavior, and $k_2v^{1/2}$ is classified as the diffusion-controlled process.[33,38–40] Therefore, the currents from the surface-controlled process region and the diffusion-controlled process region could be quantitatively calculated as shown in Fig. 6e. The pseudocapacitive contributions in the CV profiles with the scan rates of 0.1, 0.3, 0.5, and 0.8 mV s^{-1} are shown in Fig. 6f with blue bars, showing that the ion storage behavior was mainly based on a fast charge transfer from the surface without significant multi-step ion diffusion reactions.

Such dominant surface kinetics in the SnS_2/CON-10 electrode was plausibly attributed to the synergetic characteristics between those two components. The S and N atoms in CON-10 could be electrochemically favorable active sites but most of the Li-ions were irreversibly trapped in the pristine CON-10 after the first cycle of lithiation/delithiation due to the strong interaction between the active sites and Li^+, demising the storage amount of Li^+ in the subsequent cycle (Fig. S5†). However, the ultrathin SnS_2 nanoparticles inserted in between the stacks of CON-10 sheets could prevent the self-restacking of CON-10 sheets and achieve the mechanical stability of organic frameworks, resulting in large accessible areas for the (de)insertion reaction of Li^+. This would improve ionic conductivity, and contribute to fast surface charge storage processes relative to the pristine CON-10. The possible reaction equations for SnS_2 and CON-10 in the hybrid are listed in the ESI (Fig. S5†) along with an explanation.

The cycling performance and rate capability of SnS_2/CON-10 and bare SnS_2 were investigated at various current densities ranging from 0.1, 0.3, 0.5, 0.7, 0.9 A g^{-1} to 1.0 A g^{-1} (followed by a return to 0.1 A g^{-1} from the 31st cycle), as displayed in Fig. 7. In the charge and discharge curves of SnS_2/CON-10 and bare SnS_2 (Fig. 7a and b), plateaus during charge were observed, which was caused by redox reactions as found in both CV profiles (Fig. 6a and b). Furthermore, the initial discharge/charge capacities of SnS_2/CON-10 and bare SnS_2 electrodes at the current density of 0.1 A g^{-1} were determined to be 1555.1/920.6 mA h g^{-1} and 1255.7/1219.5 mA h g^{-1}, respectively, and their initial coulombic efficiencies were calculated to be 59.2% and 97.1%, respectively. The relatively low initial coulombic efficiency of SnS_2/CON-10 in the first cycle could be attributed to the irreversible trapping of Li-ions and the formation of the SEI layer. However, the coulombic efficiency of the SnS_2/CON-10 electrode increased to 99% from the 5th cycle due to the saturation of the defect sites, where Li-ions could be irreversibly trapped from the first cycle to the 4th cycle.

At the current densities of 0.3, 0.5, 0.7, 0.9, and 1.0 A g^{-1} for each 5 cycles, the average discharge capacities of SnS_2/CON-10 were 692.8, 591.9, 526.5, 474.7, and 450.1 mA h g^{-1}, while those of bare SnS_2 were 886.8, 726.6, 603.4, 501.4, and 423.8 mA h g^{-1}. In addition, the capacity retention rates were 77.5, 66.2, 59.0, 53.1 and 50.3% compared to the reversible discharge/charge capacity (893.9/848.5 mA h g^{-1}) in the 2nd cycle of SnS_2/CON-10. On the other hand, the capacity retention rates of bare SnS_2 were 70.8, 58.0, 48.1, 40.0 and 33.8%. Additionally, during cycling with the above current densities (0.3–1.0 A g^{-1}), the SnS_2/CON-10 electrode showed higher average coulombic efficiency (98.0%) than bare SnS_2 (96.4%), implying that SnS_2/CON-10 demonstrated better cycling stability than bare SnS_2. When the current density was reverted to 0.1 A g^{-1} after the 30th cycle, the discharge/charge capacity of SnS_2/CON-10 was 550.9/686.0 mA h g^{-1}, which is higher than that of bare SnS_2 (481.5/556.3 mA h g^{-1}). Furthermore, the capacity of the SnS_2/CON-10 electrode was gradually increased upon continuous cycling, while the capacity of the bare SnS_2 electrode rapidly decreased. The discharge/charge capacity of SnS_2/CON-10 was maximized to 902.6/894.9 mA h g^{-1} at the 151th cycle, which was higher than the capacity at the second cycle (893.9/848.5 mA h g^{-1}). These results showed that the CON-10 in the SnS_2/CON-10 electrode could play an important role in maintaining enhanced cyclability during successive discharge/charge reactions.

The cycling stabilities of SnS_2/CON-10 and bare SnS_2 electrodes were further compared at current densities of 0.3 A g^{-1} and 1.0 A g^{-1} for more extended cycles (Fig. 8). In Fig. 8a and c, the plateau in the first charge/discharge profile corresponds to the SEI formation; however, irreversible discharge characteristics ranging from 0.5 to 0.1 V disappeared in subsequent cycles.

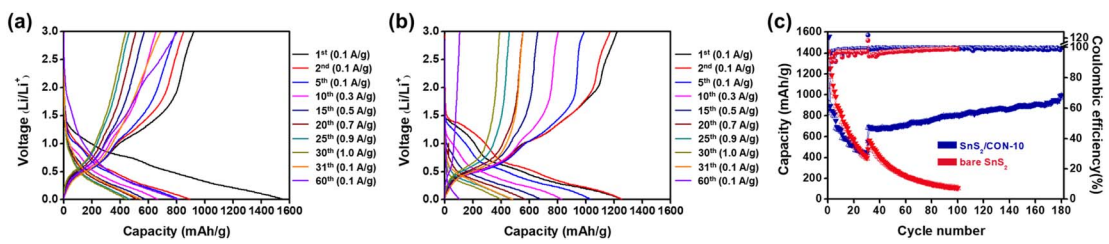

Fig. 7 Charge–discharge profiles of (a) SnS_2/CON-10 and (b) bare SnS_2 electrodes at varying current densities from 0.1 to 1.0 A g^{-1}; (c) cycling performance of SnS_2/CON-10 and bare SnS_2 electrodes at varying current densities from 0.1 to 1.0 A g^{-1}.

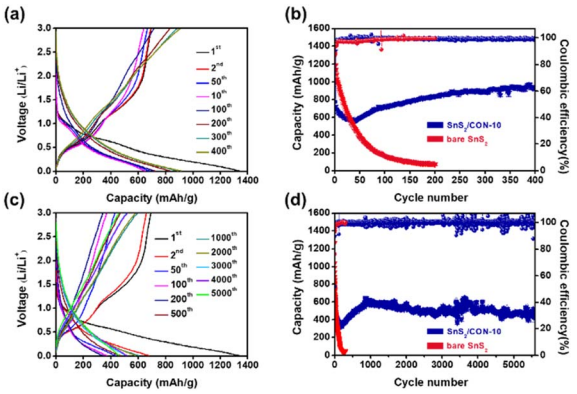

Fig. 8 Charge–discharge profiles of SnS_2/CON-10 at varying current densities of (a) 0.3 A g^{-1} and (c) 1.0 A g^{-1}; extended discharge/charge profiles of SnS_2/CON-10 and bare SnS_2 at the current density of (b) 0.3 A g^{-1} and (d) 1.0 A g^{-1}.

In addition, the shape of the charge/discharge profile for the SnS_2/CON-10 electrode at the reversible stage was almost sloped until the 5000th cycle without showing any noticeable plateau. This meant that most of the charge storage was governed by the capacitive processes at the surface of SnS_2/CON-10. Therefore, it was successfully confirmed that the physicochemical stability of the CON-10 was well preserved beyond the 5000th cycle and electrochemical reaction in the SnS_2/CON-10 electrode reversibly occurred during such long cycles.

In the case of current density of 0.3 A g^{-1}, the discharge capacity of SnS_2/CON-10 was decreased to 560.3 mA h g^{-1} until the 41st cycle, while that of bare SnS_2 continuously dropped to 74.3 mA h g^{-1} until the 200th cycle (Fig. 8b). However, after the 41st cycle, the capacity of the SnS_2/CON-10 electrode was gradually increased up to 974.6 mA h g^{-1} at the 387th cycle (Fig. 8b). This phenomenon was also observed even at a high current density such as 1.0 A g^{-1}. The capacity of SnS_2/CON-10 with the current density of 1.0 A g^{-1} was also gradually increased up to 652.4 mA h g^{-1} at the 854th cycle but that of SnS_2 was abruptly decreased to 34.0 mA h g^{-1} until around the 250th cycle under the same condition (Fig. 8d). In particular, it is worthwhile to note that SnS_2/CON-10 exhibited quite stable cycling performance for more than 5600 cycles when it was compared with the most recent SnS_2-based carbonaceous anode materials (Table S1, see ESI†). In addition, *ex situ* FTIR analysis (Fig. S6†) performed up to the 5th charge cycle revealed that the structure of CON-10 is well maintained in the SnS_2/CON-10 electrode upon discharge and charge. The SnS_2/CON-10 electrode showed an average capacity value of 507.5/506.3 mA h g^{-1} up to the 5600th cycle and stable coulombic efficiency in the range of 99–100% at the current density of 1.0 A g^{-1} (Fig. 8d). Furthermore, the structural integrities of the SnS_2/CON-10 electrode in the functioning cell after the 6550th cycle were also confirmed, as shown in Fig. S7.† However, it was hard to confirm the structural integrities of the hybrid with Raman spectroscopy (Fig. S7a†) because the vibration modes of amorphous carbons formed in SEI layers significantly contributed to the Raman spectrum of the hybrid in the cell. Nonetheless, it was successfully confirmed that SnS_2 and CON-10 structures were well maintained after the 6550th cycle with *ex situ* FTIR and PXRD (Fig. S7b and S7c†). Therefore, based on the stability information of the hybrid after long term cycling, the gradual degradation of cycling performance of the hybrid electrode up to around the 3000th cycle would be presumably caused by continuous accumulation of SEI layers and dendrites rather than decomposition of the hybrid. Although fluctuations in discharge capacity of SnS_2/CON-10 are found after 3000 cycles, it can be seen that the average discharge capacity of SnS_2/CON-10 is still well maintained even after 3000 cycles. Therefore, this implied that the heteroatoms, binding sites for Li-ions in CON-10, and the active sites in SnS_2 formed a chemically stable structure with electrolytes without seriously concerning side reactions.

Our findings suggested that the highly conductive CON-10 framework in SnS_2/CON-10 developed such excellently stable cyclic performance even at high current density *via* preventing the degradation of SnS_2 nanoparticles. Even, in Fig. 8b and d, the capacity of the SnS_2/CON-10 electrode was gradually increased in the period of few hundred cycles. At this stage, we are pursuing detailed insight into this behavior but this would presumably show the improved lithium ion diffusion kinetics during long-term cycling.

Therefore, to establish the rationale for such electrochemical behaviors observed in the cyclic performance, EIS measurements were carefully analyzed at various charged states, as shown in Fig. 9. The structural robustness together with the number of electroactive sites as Li-ion anode materials is a critical factor for efficient Li-ion diffusion kinetics and improving Li-ion storage properties. Therefore, it could be suggested that the stable and porous CON-10 as proved in the previous literature could stabilize SnS_2 nanoparticles between secondary stacks of CON-10 sheets, preventing the aggregation and pulverization of nanoparticles due to their volume change. This aspect was evident *via* comparing the impedance of bare SnS_2 measured under various charging cycle conditions at a current density of 1.0 A g^{-1}. Moreover, it can be further characterized by the distribution of relaxation times (DRT) analysis (Fig. 9 from d to f) and equivalent circuit model (ECM) fitting derived from the EIS (Fig. S8†).

The semicircles in the Nyquist plot obtained from the EIS profiles represented the overall polarization resistances. However, it was hard to distinguish and quantify each internal resistance due to the superposition of several individual resistance processes (Fig. 9a–c). Therefore, DRT analysis was performed to define internal resistances on a time scale to distinguish individual resistance processes with high resolution. For the DRT, the EIS signal in the frequency domain should have a reliable signal-to-noise ratio. In addition, the validity of the frequency-based EIS should be checked to determine whether the spectrum is linear and satisfies time invariance. Therefore, the validity of the obtained EIS for DRT analysis was determined by the Kramers–Kronig validity test through applying the following eqn (4) and (5):

$$\Delta Z' = Z'_{\text{measured}} - Z'_{\text{calculated}}|Z_{\text{calculated}}| \quad (4)$$

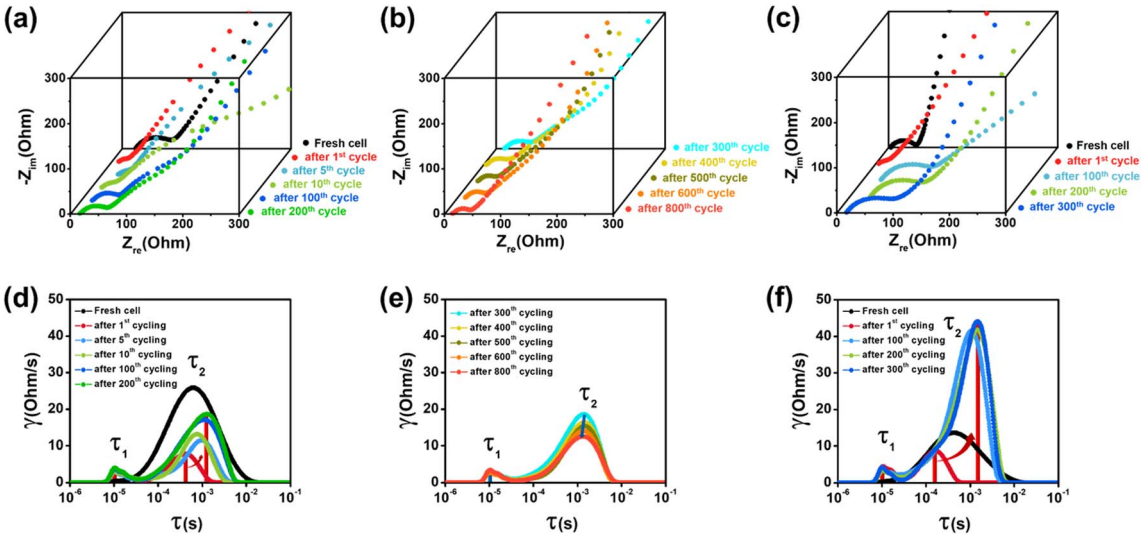

Fig. 9 Nyquist plot of the (a, b) SnS_2/CON-10 and (c) bare SnS_2 electrodes; DRT results of the (d, e) SnS_2/CON-10 and (f) bare SnS_2 electrodes.

$$\Delta Z'' = Z''_{\text{measured}} - Z''_{\text{calculated}}|Z_{\text{calculated}}| \quad (5)$$

(Z' = real part impedance and Z'' = imaginary part impedance).

We performed the Kramers–Kronig validity test using the Lin-KK tool developed by Schönleber *et al.*, and the KK residuals for all empirical impedances in the frequency range where DRT was performed were less than 1%, satisfying the Kramers–Kronig relationship (Fig. S9†).[40–44] Therefore, the signal-to-noise ratio of the impedances measured at various cycling conditions was verified for the DRT analysis. The tool for DRT analysis was in the MATLAB platform as "DRTtools" developed by Professor Francesco Ciucci *et al.*, and the code was obtained from **https://github.com/ciuccislab/**.[45] The pre-processing of empirical EIS data for DRT and the DRT conversion process were referred to previous literature, and the visualized functions obtained from DRT are successfully shown in Fig. 9d–f.[45–47]

The DRT profiles under various cyclic conditions (Fig. 9d–f) were easily identified as a static process denoted as τ_1 and a dynamic process denoted as τ_2. The film resistance (R_f) originating from electrolyte reaction and SEI formation is a typical irreversible static process and generally remains stable under various cycling conditions. The charge transfer resistance (R_{ct}) associated with charge transfer across the interface is a typical dynamic process. Besides, the peak in the τ_1 section is generally related to the thickness of the SEI layer because the resistance in τ_1 is subject to the ion transport of the SEI layer.[45–51] Therefore, since the R_f value of bare SnS_2 was approximately twice that of SnS_2/CON-10, it could be expected that the CON-10 matrix induced a stable SEI layer, alleviating side reactions between SnS_2 and electrolyte. And the thickness of the SEI layer in the SnS_2/CON-10 electrode turns out to be much thinner than that in bare SnS_2, as shown in Fig. 10a and b.

The R_f and R_{ct} values at each cycle obtained from DRT profiles for SnS_2/CON-10 and SnS_2 electrodes are summarized in Tables S2 and S3,† respectively. In the initial state from the 1st to the 200th cycle, the resistances from τ_1 and τ_2 processes in the SnS_2/CON-10 were gradually increased. After that, the resistances from τ_1 and τ_2 processes in the SnS_2/CON-10 were gradually decreased up to the 500th cycle. However, the resistances from τ_1 were quite constant through the 800th cycle, while the resistances from the τ_2 process kept decreasing to the 800th cycle (Fig. 10a and b). These resistance fluctuations quite well corresponded to the fluctuations of discharge capacity in its cyclic performance profiles, as shown in Fig. 8b and d. Nonetheless, since the amount of changes in resistances from the τ_2 process were greater than those from τ_1 and resistances from the τ_2 process kept decreasing until the 800th cycle, it could be reasonably suggested that the gradual increase in the discharge capacity up to the 800th cycle mainly relied on the alleviated resistances from the τ_2 process. However, the

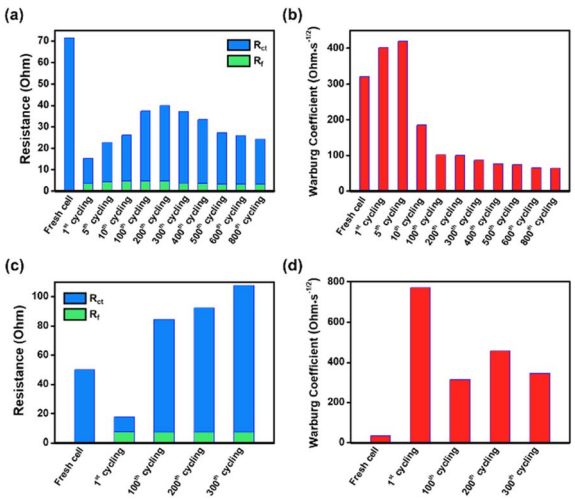

Fig. 10 (a, c) Corresponding equivalent circuit values from the model fit of the SnS_2/CON-10 and the bare SnS_2 electrode; (b, d) Warburg coefficients of the SnS_2/CON-10 electrode and the bare SnS_2. Values for each impedance parameter are shown in Tables S2 and S3.†

resistances from the τ_2 process in the bare SnS_2 quite continuously increased from the 1st cycle to 300th cycle. Furthermore, the relaxation was significantly prolonged and did not recover until the 300th cycle. The significant increase in the R_{ct} value of the bare SnS_2 electrode was concerned as the increase in interfacial transfer resistance that could be caused by the volume change and aggregation of SnS_2 particles during the repeated charge/discharge cycles (Fig. 10a and b). This would be the rationale for the capacity decrease as observed in Fig. 8d.

Therefore, it could be confirmed that the rapid surface storage processes were the prominent Li-ion storage behavior for SnS_2/CON-10, as proved in the series of CV analyses in Fig. 6. Through the DRT analysis, it could be figured out that the ion storage behavior in SnS_2/CON-10 showed the predominant surface process such as facile charge transfer rather than a complex multi-step reaction and such facile charge carrier transfer properties were successfully introduced from the highly conductive CON-10 sheets.

The Warburg diffusion region in the low-frequency region of the EIS profiles at various charge cycles could provide information on the diffusion behavior of Li-ions on the SnS_2/CON-10 and bare SnS_2 electrodes.[52–55] Therefore, their Warburg coefficients were calculated and summarized, as shown in Fig. 10b and d. The Warburg coefficient from the fresh cell with bare SnS_2 was much lower than that from the fresh cell with SnS_2/CON-10, but after the first cycling, the Warburg coefficient of bare SnS_2 was increased up to 2254% relative to that of the fresh cell. This showed the structural instability of the bare SnS_2 and the deterioration of the ion transport pathway possibly resulting from the pulverization and aggregation of particles. On the other hand, the Warburg coefficient of SnS_2/CON-10 was slightly increased to only 25% at the first cycle relative to that of the fresh cell and that value could be concerned as approximately half of the Warburg coefficient for the bare SnS_2. In addition, after the 5th cycle, the Warburg coefficient of SnS_2/CON-10 was gradually decreased to 20% of that of the fresh cell of SnS_2/CON-10 at the 800th cycle, which was just 25% of the Warburg coefficient of bare SnS_2 at the 300th cycle. As a result, it could be found that the CON-10 as the conductive matrix remained stable in the consecutive discharge/charge processes and the matrix could improve Li-ion diffusion kinetics for long cycles.

Therefore, it could be worth suggesting that the stable and conductive CON-10 in SnS_2/CON-10 facilitated both charge transfer (Fig. 10a and c) and ion transport (Fig. 10b and d) by preventing the volume change and particle aggregation of SnS_2 and providing a better ion diffusion pathway to the active sites. Besides, such characteristics of CON-10 in SnS_2/CON-10 were greatly associated with the capacity recovery in the cyclic performances (Fig. 7) and the cycling-induced capacity increase of the SnS_2/CON-10 (Fig. 8) together with high coulombic efficiency (99.5%) secured from the 100th cycle to the 800th cycle.

Experimental

Preparation of the SnS_2/CON-10 nanocomposite

The CON-10 was synthesized as reported in our previous research.[17] The SnS_2/CON-10 nanocomposite was prepared *via* a simple-one pot strategy adopted from the literatature[23] with some necessary modifications. 90 mg of CON-10 was suspended into 20 ml of *N*-methyl-2-pyrrolidone (NMP). The suspension was treated by ultrasonication for 2 hours. 0.6 g of $SnCl_2 \cdot 2H_2O$ and 0.6 g of thioacetamide (TAA) were dissolved in 10 ml of ethanol (EtOH), respectively. The $SnCl_2 \cdot 2H_2O$ solution in EtOH solution was added into CON-10 suspension and stirred for 1 hour at room temperature. Subsequently, the TAA solution in 10 ml EtOH and 20 ml of distilled water were added into the mixture of CON-10 and $SnCl_2$. The reaction mixture was stirred at 75 °C for 1 hour. The final product was recovered by centrifugation and washed with EtOH 12 times. The obtained solid product was dried at 100 °C overnight in a vacuum oven.

Preparation of bare SnS_2

SnS_2 was also synthesized by following a simple one pot strategy as described in the literature without adding graphene oxide.[23] 0.3 g of $SnCl_2 \cdot 2H_2O$ was dissolved in 25 ml of distilled water. After that, 0.3 g of TAA was added into the $SnCl_2$ solution. The reaction mixture was stirred at 75 °C for 1 hour. The final product was recovered by centrifugation and washed with distilled water and EtOH 12 times. The obtained solid product was dried at 100 °C overnight in a vacuum oven.

Characterization

Powder X-ray diffraction (XRD) patterns were obtained with a D2 phaser (Bruker) operated at 30 kV and 10 mA with Cu Kα radiation ($\lambda = 1.5406$ Å). Raman spectra were obtained with an InVia Reflex (Renishaw) with a 532 nm laser in the range of 100–2000 nm. The Fourier transform infrared (FTIR) spectra were measured on a Nicolet iS5 FT-IR spectrometer (Thermo Fisher Scientific Inc, USA). X-ray photoelectron spectroscopy (XPS) spectra were obtained with a K-Alpha (Thermo Scientific™). Field-emission scanning electron microscope (FE-SEM) images were obtained with a SU8220 (Hitachi). Field-emission transmission electron microscope (FE-TEM) images were obtained with a Titan G2 ChemiSTEM Cs Probe (FEI Company). UV-vis spectra were recorded with an Evolution™ 220 (Thermo Scientific™) in the range of 200–1100 nm, and thermogravimetric analysis (TGA) was performed under air at a heating rate of 5 °C min^{-1} from room temperature to 1000 °C with an STA 6000 (PerkinElmer). The X-ray absorption spectroscopy (XAS) experiments at Sn L_1-edge were performed at the beamlines 7D and 8C of Pohang Accelerator Laboratory (PAL, Korea). All the XAS data at Sn L_1-edge for samples were collected in the transmission mode, and the obtained data were analysed by using the IFEFFIT software package.

Electrochemical characterization

The slurries for the active electrode were prepared by mixing active materials, conductive carbon (super P), and a binder (polyacrylic acid) with a weight ratio of 7 : 2 : 1. The mixtures were carefully ground in an agate mortar and dispersed into NMP. The slurries were put on copper foil and dried at 50 °C for 1 hour. The dried active electrodes were pressed with an electric roll press (MSK-HRP-MR100DC, MTI Corporation) and dried at 100 °C for 12 hours. The final active electrodes were transferred

to a glove-box filled with argon-gas. For electrochemical analysis, half-cells were assembled with a CR2032 coin-type cell consisting of active electrodes, 3501-type separator, spacer, spring, and 1 M $LiPF_6$ as the electrolyte. The discharge/charge tests were conducted with a multichannel battery tester (Maccor K4300) in a potential window from 0.01 to 3.0 V. Cyclic voltammetry (CV) was performed with a multichannel potentiostat (WMPG1000, WonA Tech) in a potential window from 0.01 to 3.0 V. Electrochemical impedance spectroscopy (EIS) was conducted with an impedance analyser (ZiVE SP2, WonA Tech) in a frequency range from 0.01 Hz to 100 kHz. Overall electrochemical tests were operated at room temperature.

Conclusions

In the present study, we synthesized SnS_2/CON-10 by intragrowth of ultrathin SnS_2 nanoparticles within the matrices of CON-10. In particular, CON-10 played key roles in providing not only a flexible matrix preventing large volume changes and aggregation of SnS_2 nanoparticles but also good electronic conductivity. The successful incorporation of CON-10 resulted in the increase in Li ion storage capacity of the SnS_2/CON-10 electrode after thousands times of discharge/charge processes even at a high current density of 1.0 A g^{-1}. Furthermore, the recovery of capacity was rationalized by the DRT analysis, emphasizing the critical effects of employing CON-10. Therefore, our results revealed that structural properties such as large interfacial surface sites and inherent electronic properties of CON-10 were important for the cycling performances of anode materials, suggesting that the SnS_2/CON-10 could be potentially used as an advanced anode material possessing long-term cycling stability.

Author contributions

Jeong-Hun Jang: synthesis, investigation, data curation and writing-original draft; Minseop Lee: characterization, data curation and writing-review & editing; Soohyeon Park: synthesis, characterization, data curation; Jae-Min Oh: supervision, validation, writing-review & editing; Jin Kuen Park: supervision, validation, writing-review & editing; Seung-Min Paek: conceptualization, supervision, validation, and writing-review & editing.

Conflicts of interest

The authors declare no competing financial interests.

Acknowledgements

This work was supported by the National Research Foundation of Korea (NRF) funded by the South Korean Ministry of Science and ICT (Grant No. NRF-2022R1A2C1003368 and NRF-2021R1A2C1008542).

Notes and references

1 M. Armand and J.-M. Tarascon, *Nature*, 2008, **451**, 652–657.
2 Y. Shan, Y. Li and H. Pang, *Adv. Funct. Mater.*, 2020, **30**, 1–31.
3 J. P. Pender, G. Jha, D. H. Youn, J. M. Ziegler, I. Andoni, E. J. Choi, A. Heller, B. S. Dunn, P. S. Weiss, R. M. Penner and C. B. Mullins, *ACS Nano*, 2020, **14**, 1243–1295.
4 N. Du, X. Wu, C. Zhai, H. Zhang and D. Yang, *J. Alloys Compd.*, 2013, **580**, 457–464.
5 Q. Wang, Y. X. Nie, B. He, L. L. Xing and X. Y. Xue, *Solid State Sci.*, 2014, **31**, 81–84.
6 M. H. Modarres, J. H.-W. Lim, C. George and M. De Volder, *J. Phys. Chem. C*, 2017, **121**, 13018–13024.
7 Y. Zhang, Y. Guo, Y. Wang, T. Peng, Y. Lu, R. Luo, Y. Wang, X. Liu, J. K. Kim and Y. Luo, *Nanoscale Res. Lett.*, 2018, **13**, 389.
8 Y. Jiang, D. Song, J. Wu, Z. Wang, S. Huang, Y. Xu, Z. Chen, B. Zhao and J. Zhang, *ACS Nano*, 2019, **13**, 9100–9111.
9 H. S. Kim, Y. H. Chung, S. H. Kang and Y. E. Sung, *Electrochim. Acta*, 2009, **54**, 3606–3610.
10 P. J. Yen, P. R. Ilango, Y. C. Chiang, C. W. Wu, Y. C. Hsu, Y. L. Chueh and K. H. Wei, *Mater. Today Energy*, 2019, **12**, 336–347.
11 T. Hu, X. Sun, H. Sun, G. Xin, D. Shao, C. Liu and J. Lian, *Phys. Chem. Chem. Phys.*, 2014, **16**, 1060–1066.
12 X. Chen, Y. Huang, K. Zhang, X. S. Feng and M. Wang, *Chem. Eng. J.*, 2017, **330**, 470–479.
13 Q. Sun, D. Li, L. Dai, Z. Liang and L. Ci, *Small*, 2020, **16**, 1–10.
14 H. Sun, M. Ahmad, J. Luo, Y. Shi, W. Shen and J. Zhu, *Mater. Res. Bull.*, 2014, **49**, 319–324.
15 L. Wu, J. Zheng, L. Wang, X. Xiong, Y. Shao, G. Wang, J. H. Wang, S. Zhong and M. Wu, *Angew. Chem., Int. Ed.*, 2019, **58**, 811–815.
16 A. V. Desai, R. E. Morris and A. R. Armstrong, *ChemSusChem*, 2020, **13**, 4866–4884.
17 M. S. Kim, W. J. Lee, S. M. Paek and J. K. Park, *ACS Appl. Mater. Interfaces*, 2018, **10**, 32102–32111.
18 M. S. Kim, M. Lee, M. J. Kim, Y. K. Jeong, J. K. Park and S. M. Paek, *J. Mater. Chem. A*, 2020, **8**, 17790–17799.
19 M. Lee, M. S. Kim, J. M. Oh, J. K. Park and S. M. Paek, *ChemSusChem*, 2021, **14**, 3244–3256.
20 M. S. Kim, C. S. Phang, Y. K. Jeong and J. K. Park, *Polym. Chem.*, 2017, **8**, 5655–5659.
21 W. C. Ko, M. S. Kim, Y. J. Kwon, J. Jeong, W. R. Kim, H. Choi, J. K. Park and Y. K. Jeong, *J. Mater. Chem. A*, 2020, **8**, 19246–19253.
22 M. S. Kim, T. H. Gu, S. Park, T. Kim, Y. K. Jo, Y. K. Jeong, J. K. Park and S. J. Hwang, *J. Mater. Chem. A*, 2022, **10**, 15508–15519.
23 X. Li, X. Sun, Z. Gao, X. Hu, R. Ling, S. Cai, C. Zheng and W. Hu, *ChemSusChem*, 2018, **11**, 1549–1557.
24 C. F. Holder and R. E. Schaak, *ACS Nano*, 2019, **13**, 7359–7365.
25 A. J. Smith, P. E. Meek and W. Y. Liang, *J. Phys. C Solid State Phys.*, 1977, **10**, 1321–1333.
26 J. M. Gonzalez and I. I Oleynik, *Chem. Phys. Rev. B*, 2016, **94**, 125443–125453.
27 J. Johny, S. Sepulveda-Guzman, B. Krishnan, D. Avellaneda and S. Shaji, *Appl. Surf. Sci.*, 2018, **435**, 1285–1295.
28 P. Li, W. Fu, P. Zhuang, Y. Cao, C. Tang, A. B. Watson, P. Dong, J. Shen and M. Ye, *Small*, 2019, **15**, 1–8.

29 H. Mukaibo, A. Yoshizawa, T. Momma and T. Osaka, *J. Power Sources*, 2003, **119–121**, 60–63.
30 Y. Jiang, Y. Feng, B. Xi, S. Kai, K. Mi, J. Feng, J. Zhang and S. Xiong, *J. Mater. Chem. A*, 2016, **4**, 10719–10726.
31 Y. Q. Wu, Y. Yang, H. Pu, R. Z. Gao, W. J. Meng, H. X. Yang and D. L. Zhao, *J. Alloys Compd.*, 2020, **822**, 153686.
32 P. Zheng, Z. Dai, Y. Zhang, K. N. Dinh, Y. Zheng, H. Fan, J. Yang, R. Dangol, B. Li, Y. Zong, Q. Yan and X. Liu, *Nanoscale*, 2017, **9**, 14820–14825.
33 J. Liu, J. Wang, C. Xu, H. Jiang, C. Li, L. Zhang, J. Lin and Z. X. Shen, *Adv. Sci.*, 2018, **5**, 1700322.
34 X. Wang, D. Chen, Z. Yang, X. Zhang, C. Wang, J. Chen, X. Zhang and M. Xue, *Adv. Mater.*, 2016, **28**, 8645–8650.
35 S. Liu, L. Kang, J. Hu, E. Jung, J. Zhang, S. C. Jun and Y. Yamauchi, *ACS Energy Lett.*, 2021, **6**, 3011–3019.
36 J. Chen, B. Liu, H. Cai, S. Liu, Y. Yamauchi and S. C. Jun, *Small*, 2023, **19**, 2204275.
37 L. Kang, M. Zhang, J. Zhang, S. Liu, N. Zhang, W. Yao, Y. Ye, C. Luo, Z. Gong, C. Wang, X. Zhou, X. Wu and S. C. Jun, *J. Mater. Chem. A*, 2020, **8**, 24053–24064.
38 V. Augustyn, P. Simon and B. Dunn, *Energy Environ. Sci.*, 2014, **7**, 1597–1614.
39 C. Choi, D. S. Ashby, D. M. Butts, R. H. DeBlock, Q. Wei, J. Lau and B. Dunn, *Nat. Rev. Mater.*, 2020, **5**, 5–19.
40 M. Lee, M.-S. Kim, J.-M. Oh, J. K. Park and S.-M. Paek, *ACS Nano*, 2023, **17**, 3019–3036.
41 M. Schönleber, D. Klotz and E. Ivers-Tiffée, *Electrochim. Acta*, 2014, **131**, 20–27.
42 B. A. Boukamp, *J. Electrochem. Soc.*, 1995, **142**, 1885–1894.
43 M. Schönleber and E. Ivers-Tiffée, *Electrochem. Commun.*, 2015, **58**, 15–19.
44 B. Manikandan, V. Ramar, C. Yap and P. Balaya, *J. Power Sources*, 2017, **361**, 300–309.
45 T. H. Wan, M. Saccoccio, C. Chen and F. Ciucci, *Electrochim. Acta*, 2015, **184**, 483–499.
46 K. Pan, F. Zou, M. Canova, Y. Zhu and J. H. Kim, *J. Power Sources*, 2020, **479**, 229083.
47 J. Illig, M. Ender, T. Chrobak, J. P. Schmidt, D. Klotz and E. Ivers-Tiffée, *J. Electrochem. Soc.*, 2012, **159**, A952–A960.
48 X. Zhou, Z. Pan, X. Han, L. Lu and M. Ouyang, *J. Power Sources*, 2019, **417**, 188–192.
49 Y. Lu, C. Z. Zhao, R. Zhang, H. Yuan, L. P. Hou, Z. H. Fu, X. Chen, J. Q. Huang and Q. Zhang, *Sci. Adv.*, 2021, **7**, 1–11.
50 X. Zhou, J. Huang, Z. Pan and M. Ouyang, *J. Power Sources*, 2019, **426**, 216–222.
51 P. Shafiei Sabet, A. J. Warnecke, F. Meier, H. Witzenhausen, E. Martinez-Laserna and D. U. Sauer, *J. Power Sources*, 2020, **449**, 227369.
52 P. Vadhva, J. Hu, M. J. Johnson, R. Stocker, M. Braglia, D. J. L. Brett and A. J. E. Rettie, *ChemElectroChem*, 2021, **8**, 1930–1947.
53 M. Gaberšček, *Nat. Commun.*, 2021, **12**, 19–22.
54 J. Moškon and M. Gaberšček, *J. Power Sources Adv.*, 2021, **7**, 100047.
55 M. D. Levi, V. Dargel, Y. Shilina, D. Aurbach and I. C. Halalay, *Electrochim. Acta*, 2014, **149**, 126–135.